

1 **Exfoliated transition metal dichalcogenide (TMD) nanosheets for supercapacitor and**  
2 **sodium ion battery applications**  
3

4 *Santanu Mukherjee<sup>a</sup>, Jonathan Turnley<sup>a</sup>, Elisabeth Mansfield<sup>b</sup>, Jason Holm<sup>b</sup>, Davi Soares<sup>a</sup>,*  
5 *Lamuel David<sup>a</sup> and Gurpreet Singh<sup>a\*</sup>*

6  
7  
8  
9  
10  
11  
12  
13  
14  
15  
16  
17  
18  
19 <sup>a</sup>Department of Mechanical and Nuclear Engineering, Kansas State University, KS, USA, 66506  
20 <sup>b</sup>National Institute of Standards and Technology, Boulder, CO, USA, 80305  
21  
22  
23  
24  
25

26 \*Corresponding author: [gurpreet@ksu.edu](mailto:gurpreet@ksu.edu)

## Abstract

Growing concerns regarding the safety, flammability, and hazards posed by Li-ion systems have led to research on alternative rechargeable metal-ion electrochemical storage technologies. Among the most notable of these are Na-ion supercapacitors and batteries, motivated in part because of the similar size and electrochemistry of Li and Na ions. However, sodium ion batteries (SIBs) come with their own set of issues, especially the large size of the  $\text{Na}^+$  ion, its relatively sluggish kinetics and low energy densities. This makes the development of novel materials and appropriate electrode architecture is of absolute significance. Transition metal dichalcogenides (TMDs), in this regard have attracted a lot of attention due of their relative ease of exfoliation, diverse morphologies and architectures with superior electronic properties. Here, we study the electrochemical performance of Mo based two dimensional (2D) layered TMDs (e.g.  $\text{MoS}_2$ ,  $\text{MoSe}_2$ , and  $\text{MoTe}_2$ ), exfoliated in a superacid, for battery and supercapacitor applications. The exfoliated TMD flakes were interfaced with reduced graphene oxide (rGO) to be used as composite electrodes. Electron microscopy, elemental mapping, Raman spectra were used to analyze the exfoliated material and confirm the formation of 2D TMD/rGO layer morphology. For supercapacitor applications in aqueous media, the sulfide-based TMD ( $\text{MoS}_2$ ) exhibited the best performance, providing an areal capacitance of  $60.25 \text{ mF cm}^{-2}$ . For SIB applications, TMD electrodes exhibited significantly high charge capacities than the neat rGO electrode. The initial desodiation capacities for the composite electrodes  $468.84 \text{ mAh g}^{-1}$  ( $1687.82 \text{ C g}^{-1}$ ),  $399.10 \text{ mAh g}^{-1}$  ( $1436.76 \text{ C g}^{-1}$ ) and  $387.36 \text{ mAh g}^{-1}$  ( $1394.49 \text{ C g}^{-1}$ ) for  $\text{MoS}_2$ ,  $\text{MoSe}_2$ , and  $\text{MoTe}_2$  respectively. Also, all the composite TMD electrodes provided a coulombic efficiency of  $\sim 100 \%$  after few cycles.

## 1 **Introduction**

2 Batteries and supercapacitors are being considered for powering an increasingly diverse range of  
3 applications from stationary solar/wind energy farms, to flexible and wearable electronic devices like  
4 wearable electronics and microchips [1]. To date, lithium-ion rechargeable systems have been at the  
5 forefront of devices for energy storage applications [2, 3]. Advantages of Li-ion systems include the  
6 easy and reversible Li intercalation-deintercalation reaction due to lithium's small ionic size, portability  
7 and reasonably high volumetric energy densities [4, 5]. However, Li-ion rechargeable systems also  
8 have their share of drawbacks, including the high cost of Li metal, flammability, undesirable side  
9 reactions, and the formation of unwanted solid electrolyte interface (SEI) layers to name a few [6, 7].  
10 The high cost of Li especially hinders applications where large quantities are needed, i.e. in medium-  
11 and large-scale grid storage applications [8]. These drawbacks have encouraged an ongoing search for  
12 non-Li-ion based rechargeable energy storage devices, among which Na, Mg, Al and K-ion systems are  
13 at the forefront [9-11]. Out of these, Na-ion rechargeable systems have received increasing attention  
14 because as opposed to Li, Na resources are practically inexhaustible and evenly distributed around the  
15 world [8, 12-14]. Also, since Na and Li are both alkali metals, it is likely that electrode materials for Li  
16 can be utilized for Na-ion systems [15]. A simple exchange, however, is not necessarily straightforward  
17 because Na and other metal-ions are much larger than Li-ions, and electrode designs must be altered  
18 to accommodate: (a) their slow diffusion kinetics in the bulk, and (b) structural changes in host the  
19 material associated with large volume changes upon bulky Na-ion insertion/extraction that causes  
20 capacity degradation [16, 17].

21 As noted above, the application of Na-ions as charge carriers imposes unique limitations on the  
22 electrode material, and therefore the design and development of novel materials and their architectures  
23 are of absolute importance [18]. Transition metal dichalcogenides (TMDs) have drawn significant  
24 research attention lately because of their unique properties [19-21]. This class of materials can offer  
25 two dimensional (2D) layered morphologies that exhibit large surface areas, and enhanced  
26 electrochemical kinetics coupled with low volume changes upon ionic intercalation. For example,

1 Balasingam et al. studied few-layered MoSe<sub>2</sub> nanosheets prepared by hydrothermal techniques for  
2 supercapacitor applications<sup>20</sup>. An optimum capacitance of 49.7 F g<sup>-1</sup> was obtained with a 75 %  
3 capacitance retention after 10,000 cycles of operation. WS<sub>2</sub> "nanoribbons" have been studied as a  
4 supercapacitor electrode in a potassium electrolyte, and results have indicated the 1T atomic  
5 configuration to perform better than its 2H counterpart [22]. The 1T nanoribbon produced an optimum  
6 areal capacitance of 2813 μF cm<sup>-2</sup> which was about 12 times greater than the 2H type [22]. A recent  
7 report on MoS<sub>2</sub> (a variety of TMD) electrodes for Na-ion batteries showed double the capacity value of  
8 the Na/MoS<sub>2</sub> theoretical insertion value [23]. This observation is important because graphite, which  
9 can also exhibit 2D layered morphology, exhibits almost negligible capacity and cyclability toward Na  
10 [24]. It was speculated that a conversion-type reaction could be responsible for high capacity. MoSe<sub>2</sub>  
11 nanoplates have been studied as anodes in sodium ion batteries (SIBs). The nanoplates were fabricated  
12 by pyrolysis and initial charge and discharge capacities of 1400 C g<sup>-1</sup> and 1846.8 C g<sup>-1</sup> were obtained  
13 at a rate of 0.1 C. However, the capacity decayed to about 1400 C g<sup>-1</sup> after 50 cycles of operation. The  
14 reduction was attributed to change in lattice structure of MoSe<sub>2</sub> from octahedron to a tetrahedral due  
15 to Na ion intercalation [25]. David et al. have studied MoS<sub>2</sub>/graphene composite free standing anodes  
16 in SIB systems [23]. Their composite anode demonstrated a stable charge capacity of 828 C g<sup>-1</sup> with a  
17 99 % coulombic efficiency.

18 A detailed comparative study of the family of TMDs, especially as electrodes in sodium ion  
19 supercapacitor systems, is lacking in the literature. In this manuscript, a novel superacid-assisted  
20 exfoliation technique is utilized to study the electrochemical behavior of TMDs as potential electrode  
21 materials for sodium ion supercapacitors and batteries. This manuscript, therefore, aims to study the  
22 effect of exfoliating these materials in a novel way, as well as to study their viability as energy storage  
23 materials and to probe into their electrochemical phenomena under both aqueous and organic  
24 electrolyte environments.

## 1 **Experimental**

### 2 **Synthesis of exfoliated or acid-treated TMD nanosheets**

3 TMD powders (99 %, Sigma Aldrich)<sup>1</sup> were sonicated for 30 minutes in concentrated superacid (pH <  
4 -1 and density 1.75 g ml<sup>-1</sup>, Sigma™) to form a solution (concentration of solution  $\approx$  2 mg mL<sup>-1</sup>) for  
5 exfoliating TMD flakes. Two types of superacids were used: chlorosulfonic acid (superacid, 99%, Sigma  
6 Aldrich) and methanesulfonic acid. Note that the superacid was added *very slowly* (so as to prevent a  
7 exothermic reaction) to the TMD powder in an argon-filled glovebox (dew point  $-50$  °C, the low dew  
8 point being necessary so that the moisture content is minimal as superacid will be used). The solution  
9 was then carefully quenched in 1.0 L of distilled water (performed with extreme caution in a glovebox).  
10 Additional dilution with DI water was done to reduce the solution acidity. The supernatant containing  
11 the (lighter) exfoliated flakes was pipetted from the top portion of the solution and dried in a  
12 conventional oven to obtain dry superacid treated TMD nanosheets. This process is based on the  
13 rationale that the protonation of the TMDs in solution (by the dissociation of the chlorosulfonic acid),  
14 coupled with the sonication, provides energy necessary to overcome the weak van der Waals forces of  
15 attraction between the bulk TMD sheets.

### 16 **Synthesis of graphene oxide (GO)**

17 Sodium nitrate, potassium permanganate, sulfuric acid, hydrogen peroxide (31.3 % solution in water),  
18 hydrochloric acid (30 % solution in water), methanol (99.9 %) were purchased from Fisher Scientific.  
19 All materials were used as received without further purification. Hummer's method was used to make  
20 graphene oxide [26].  
21

### 22 **Synthesis of rGO/TMD composite paper**

23 15 mg GO and 22.5 mg of acid-treated TMD nanosheets were added to a 1:1 volume fraction solution  
24 of water and isopropanol. The mixture was sonicated for 60 min (Branson Sonifier) to disperse the  
25

---

<sup>1</sup> *Certain commercial equipment, instruments, or materials are identified in this paper in order to specify the experimental procedure adequately. Such identification is not intended to imply recommendation or endorsement by the National Institute of Standards and Technology, nor is it intended to imply that the materials or equipment identified are necessarily the best available for the purpose*

1 nanosheets in the solution. The composite suspension was then vacuum filtered using a 47 mm  
2 diameter, 10  $\mu\text{m}$  pore size, filter membrane (HPLC grade, Millipore). TMD/GO composite paper thus  
3 obtained was dried in an oven at 70  $^{\circ}\text{C}$  overnight and subsequently reduced at 500  $^{\circ}\text{C}$  for 2 h, and  
4 again at 900  $^{\circ}\text{C}$  for 5 min in argon. The samples are denoted hereafter as rGO for neat rGO, and  $\text{MoS}_2$ ,  
5  $\text{MoSe}_2$ , and  $\text{MoTe}_2$  for the respective TMDs, each of which comprises approximately 20% by mass rGO  
6 as conducting agent.

### 7 **Instrumentation for structural characterization**

9 Transmission electron microscope (TEM) images were digitally acquired by use of a Phillips CM100  
10 operated at 100 kV. Raman spectroscopy was performed by a Horiba Jobin Yvon LabRam ARAMIS  
11 confocal Raman microscope using a He-Ne laser ( $\sim 632.8$  nm). Energy dispersive spectra (EDS) were  
12 collected using a Zeiss Gemini scanning electron microscope (SEM) at 10-30 keV. To observe the  
13 layered electrode morphology cross-section, a focused  $\text{Ga}^+$  ion beam (Zeiss Auriga FIB-SEM) was used  
14 to cut notches at the edges of the exfoliated TMD composite structures.

### 16 **Fabrication of electrodes, cell assembly and electrochemical testing**

17 For use in *supercapacitors in aqueous media*, 20-30 mg of active material (TMD powder) were thoroughly  
18 ground with 5 % by mass PVDF (binder) and C black (for improving electronic conductivity) each. The  
19 grinding was done in a mortar-pestle with the dropwise addition of N-methyl pyrrolidone (NMP) solvent  
20 such that a viscous slurry was obtained with a "honey-like" consistency. The slurry was then pasted on  
21 stainless steel substrates and dried overnight in a box-furnace at 55  $^{\circ}\text{C}$ . For electrochemical testing as  
22 supercapacitors, a 3-electrode setup was used with a Pt wire counter-electrode, and an Ag/AgCl reference  
23 electrode in a 1M aqueous  $\text{Na}_2\text{SO}_4$  electrolyte. Cyclic voltammetry (CV) was performed within a range of  
24 0.0-0.8 V at scan rates of 5, 50, 100, 200 and 500  $\text{mV s}^{-1}$  respectively, using a CHI™ 660 E electrochemical  
25 workstation. This same workstation was used for performing electrochemical impedance spectroscopy  
26 (EIS) in 1M aqueous  $\text{Na}_2\text{SO}_4$  solution. Galvanostatic charge-discharge (GCD) was performed at current  
27 densities of 0.5, 1.0, 1.5 and 2.0  $\text{mA cm}^{-2}$  respectively using the same workstation. The set-up of the 3-

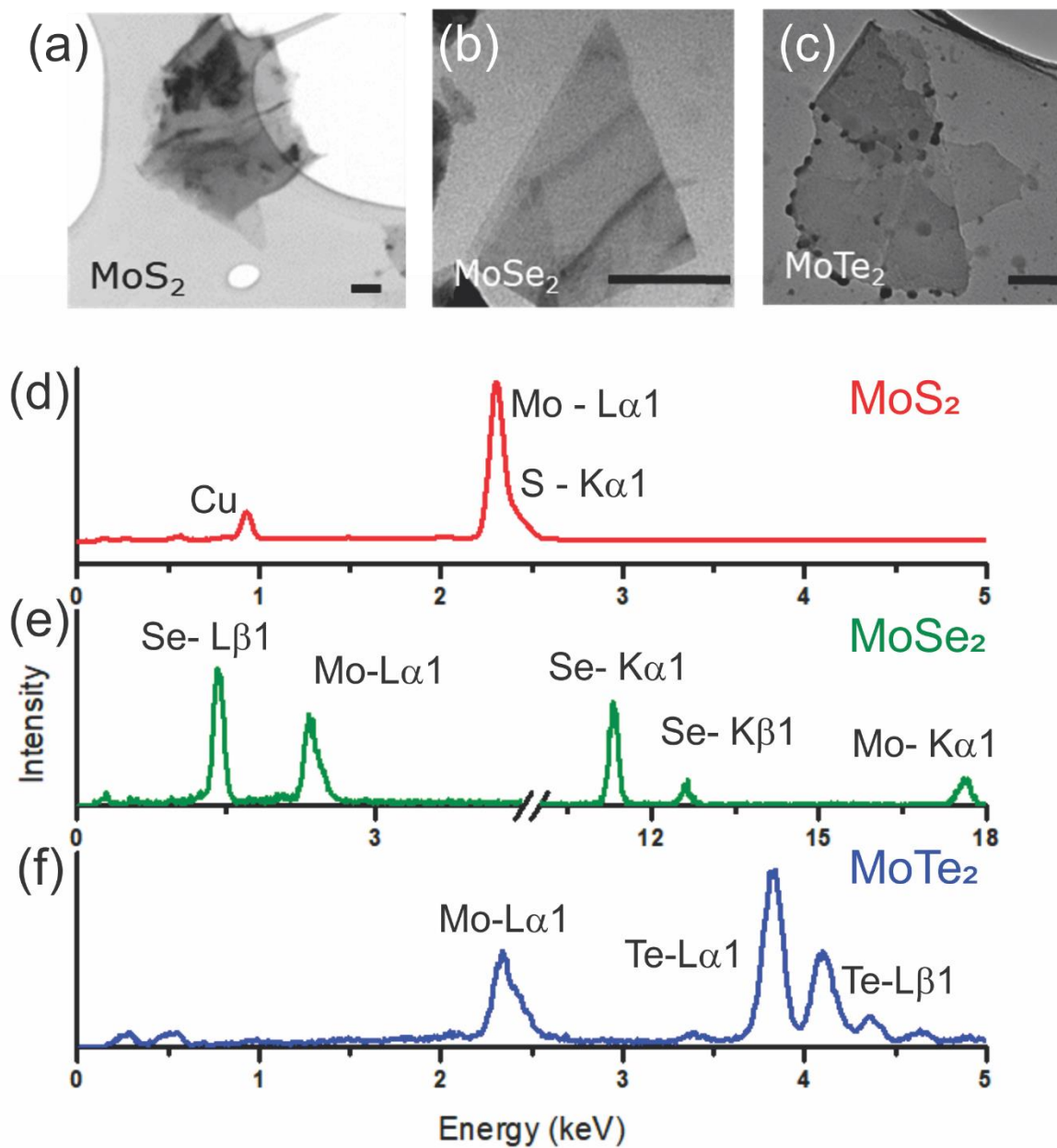
1 electrode system is such that the electrode needs to be supported by a clip and a free standing electrode's  
2 structural integrity was compromised under the tensile stress from the clip. Hence, a stainless steel current  
3 collector was used during this testing.

4 For applications in *batteries in organic media*, the free standing rGO/TMD composite papers were used  
5 directly as the working electrodes. 14.3 mm diameter electrodes were punched out of the composite  
6 paper. Electrochemical analysis was performed using coin cells (CR 2032) and a two-electrode setup  
7 was employed. 1M NaClO<sub>4</sub> (Alfa Aesar) in (1:1 volume fraction) dimethyl carbonate:ethylene carbonate  
8 (DMC:EC) served as the electrolyte. A 25 μm thick glass separator soaked in electrolyte was placed  
9 between the working electrode and pure Na metal (14.3 mm diameter, 75 μm thick) used as the  
10 counter-electrode. GCD analysis was performed between 2.25 V and 10 mV versus Na/Na<sup>+</sup> using a  
11 multichannel BT2000 Arbin test unit.  
12

## 13 **Results and Discussion**

### 14 **Structural and phase characterization**

#### 15 **TEM imaging and EDS**

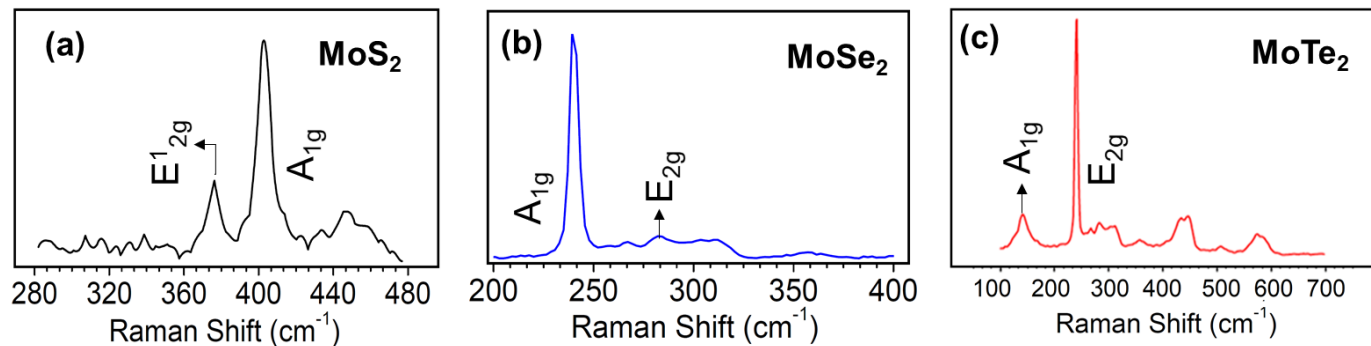


1  
2  
3 **Figure 1. TEM micrographs and EDS of the exfoliated TMD samples.** (a), (b) and (c) are TEM images of  
4 the exfoliated TMD samples exhibiting a homogenous multi-layered nanosheet morphology. Scale bars = 100 nm,  
5 (d) EDS of the MoS<sub>2</sub> sample demonstrating the characteristic Mo and S peaks, along with a Cu peak from the  
6 substrate (e) EDS of the MoSe<sub>2</sub> sample demonstrating the characteristic Mo and Se peaks, (f) EDS of the MoTe<sub>2</sub>  
7 sample indicating characteristic Mo and Te peaks.

1  
2 TEM imaging is necessary to understand not only the structure and morphology of the exfoliated sheets,  
3 but also to observe whether the acid based exfoliation process has been successful in providing the sheet  
4 like microstructure that is desired. The TEM images of the exfoliated TMD samples in Fig. 1(a)–(c)  
5 demonstrate the formation of triangular or rhomboidal shaped sheets. The images indicate the formation  
6 of a stacked, few-layered morphology and the absence of single-layered flakes can be attributed to the  
7 volume/morphology of the bulk TMD precursor, the type and strength of acid used, and the power used  
8 during the sonication process [27]. Optimization of the sonication process should be able to provide a  
9 direct correlation with number of layers and the type of morphology obtained. Also, the observation that  
10 the flakes range in linear dimensions between 50-100 nm is consistent with earlier work by the same  
11 group [23]. The exfoliated TMD sample images demonstrate a homogenous and defect-free morphology,  
12 especially at the sheet edges. It can be inferred from these observations that the homogenous nature of  
13 the flaky and rigid nanosheets will tend to prevent their restacking and maintain their 2D morphology  
14 throughout the cell cycling. It is also pertinent to note that in Fig 1(c), some dots are observed at the  
15 edge of the MoTe<sub>2</sub> sample. These dots seen at the edge of the MoTe<sub>2</sub> can have two probabilities. Firstly,  
16 it can be hypothesized that very small amounts of the exfoliated MoTe<sub>2</sub> may have restacked together.  
17 This is a feature of exfoliated TMDs and a similar appearance has also been reported in the literature [28,  
18 29]. Secondly, it is also possible that all of the bulk MoTe<sub>2</sub> obtained commercially may not have been in  
19 layered form and there may have been a very small fraction in a non-layered form. Consequently, on  
20 exfoliation, these non-layered parts did not exfoliate out and are observed as particulate “dots” in the  
21 TEM. Of course, they are a very small fraction of the entire sample and the TEM image proves that.  
22 Fig. 1(d) shows an EDS of the exfoliated MoS<sub>2</sub> sample where characteristic Mo and S peaks (L $\alpha$  and K $\alpha$ )  
23 can be observed. Fig. 1(e)-(f) similarly show EDS survey spectra of the exfoliated MoS<sub>2</sub>, MoSe<sub>2</sub> and the  
24 exfoliated MoTe<sub>2</sub> samples. The characteristic Mo (K $\alpha$  and L $\alpha$ ) and Se (K $\alpha$ , K $\beta$  and L $\beta$ ) and Te (L $\alpha$  and  
25 L $\beta$ ) spectral lines can be observed. Another important observation is the absence of any impurity peaks,  
26 especially Cl peaks from residual chlorosulfonic acid. This indicates phase purity of the exfoliated

1 samples, thereby further confirming the results seen in the Raman spectra for these samples. However,  
2 it is understood that there may be some trace amounts of  $\text{Cl}^-$  which is beyond the resolution limit of  
3 the EDX instrument.

## 4 Raman spectra



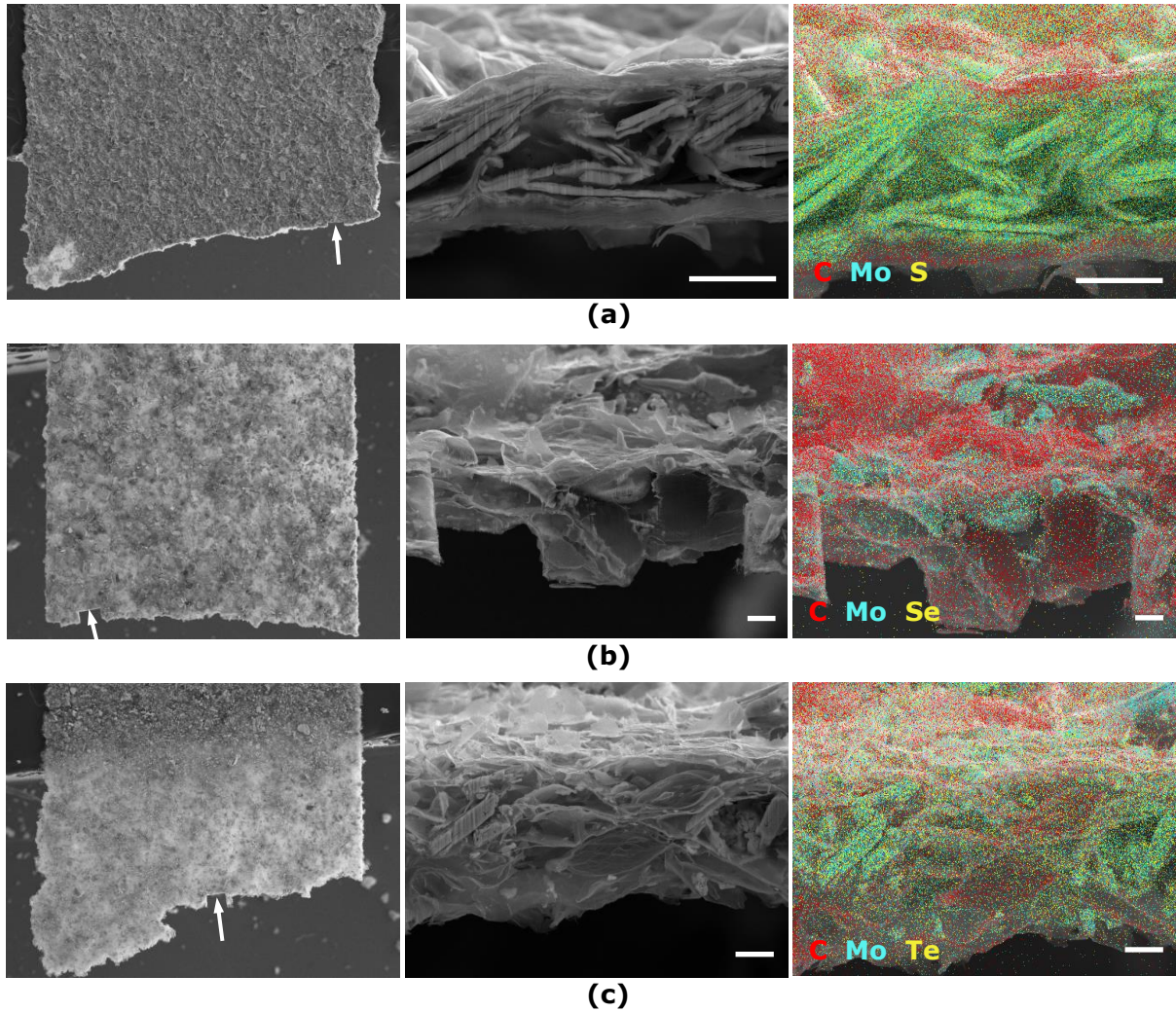
7 **Figure 2. Raman spectra of the exfoliated TMD samples. (a), (b) and (c)** are the Raman spectra of the  
8 exfoliated MoS<sub>2</sub>, MoSe<sub>2</sub> and MoTe<sub>2</sub> samples. The characteristic vibration modes of the sample (A<sub>1g</sub> and E<sub>2g</sub>)  
9 corresponding to their out-of-plane and in-plane vibrations, seen as peaks in the spectra have been labeled for  
10 the respective TMDs.

11  
12 Fig. 2 (a)-(c) show Raman spectra of the exfoliated MoS<sub>2</sub>, MoSe<sub>2</sub>, and MoTe<sub>2</sub> respectively.  
13 Characteristic E<sub>2g</sub> and A<sub>1g</sub> peaks can be observed for all the samples. The A<sub>1g</sub> mode indicates the out-  
14 of-plane vibration of the chalcogen species, whereas the E<sub>2g</sub> mode is an indicator of in-plane vibrations  
15 of the Mo species [30]. Note that the observed sharp peaks of the A<sub>1g</sub> modes are mainly due to the  
16 interaction of the incident laser beam with the direct band gap, resulting in resonance [31, 32]. The  
17 peak positions also indicate the formation few-layered samples. For only a monolayer, there is only  
18 one active vibrational mode that can be usually observed. However, for the MoSe<sub>2</sub> sample, the A<sub>1g</sub>  
19 mode at 240 cm<sup>-1</sup> is visible as a sharp peak in Fig. 2(b). Also, the E<sub>12g</sub> and the A<sub>1g</sub> modes are observed  
20 in all the cases, indicating the existence of several layers. This is especially true for the MoTe<sub>2</sub> sample,  
21 which shows several auxiliary peaks indicating the formation of multiple layers [33].

22 The absence of impurity peaks demonstrate that the superacid-based exfoliation process has not

1 resulted in the dissolution of sulfur or formation of impurity phases. EDS results in the next section  
2 support this conclusion.

### 3 **Cross-sectional imaging and elemental mapping of the exfoliated layers**



4 **Figure 3. Images and elemental maps of the exfoliated, layered structures: (a) MoS<sub>2</sub>, (b) MoSe<sub>2</sub>, and**  
5 **(c) MoTe<sub>2</sub>.** Each set of three images shows a low magnification survey image (left, with arrows indicating the  
6 100 nm wide FIB-milled notch), a cross-section view of the structure (middle), and an X-ray map (right) with  
7 inset element color key. Scale bars are 10 μm.  
8  
9

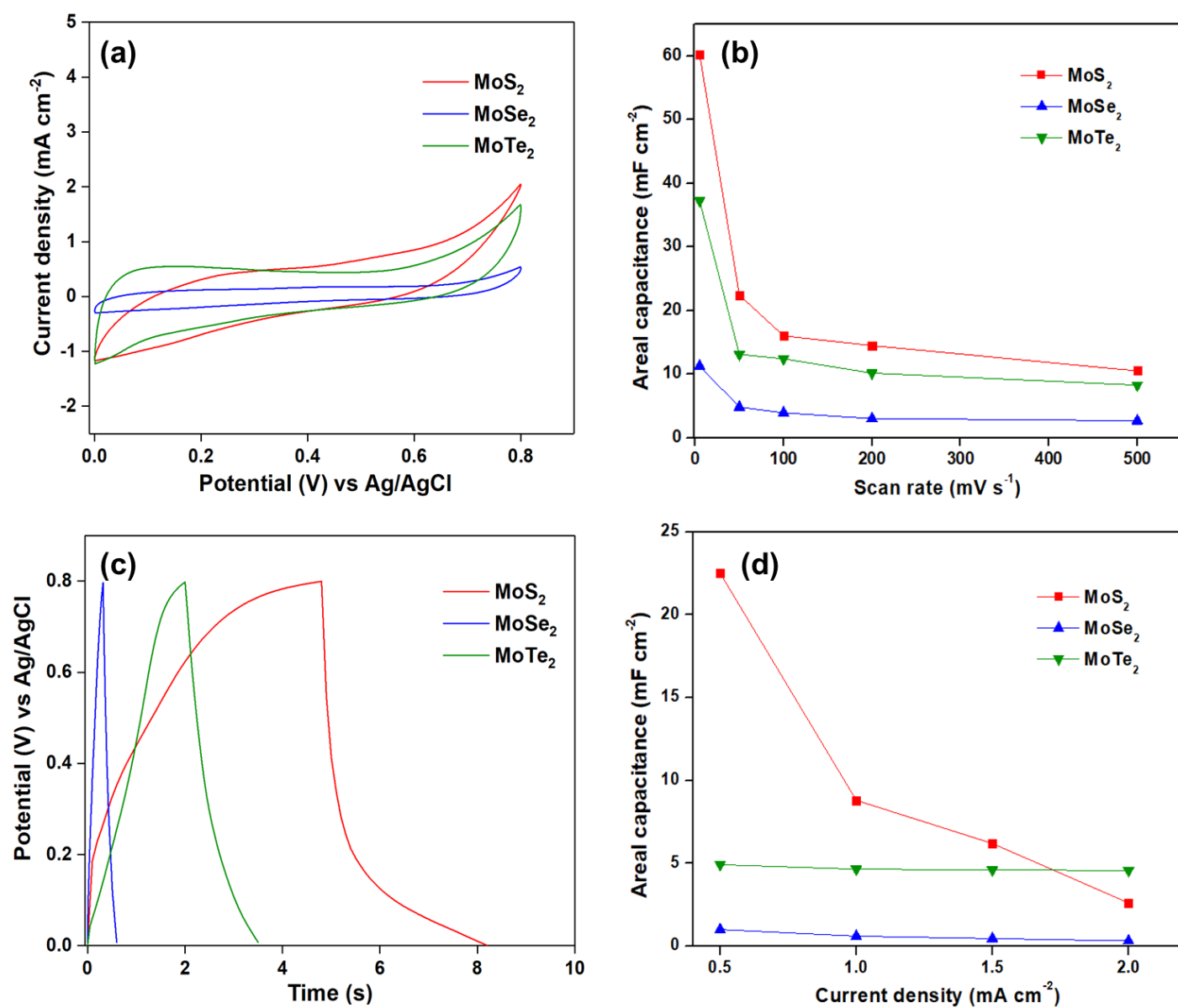
10 Figure 3 shows the 2D exfoliated TMD sample structures in greater detail. The MoS<sub>2</sub>, MoSe<sub>2</sub>, and MoTe<sub>2</sub>  
11 samples are shown in Figure 3(a), 3(b), and 3(c), respectively. Images on the left are low-magnification

1 secondary electron images, in which each sample exhibits a uniform appearance over a large area. The  
2 white arrows point to 100  $\mu\text{m}$  wide notches FIB-milled into small pieces of each of the three exfoliated  
3 TMD samples. Images in the middle show the notch cross-section where the layered morphology and  
4 individual flakes of the TMD material can be observed. Images on the right show X-ray maps  
5 superimposed on the secondary electron images. The X-ray maps and the cross-sectional images  
6 suggest that the exfoliated  $\text{MoS}_2$  sample exhibits a distinct layered morphology compared to the  $\text{MoSe}_2$   
7 and  $\text{MoTe}_2$  samples, with several TMD flakes sandwiched between rGO layers . It is important to note  
8 the X-ray maps suggest the composition is relatively uniform. If individual "islands" had been observed  
9 throughout the flake, this could have contributed to inhomogeneities that would be detrimental towards  
10 electrochemical performance.

## 11 **Electrochemical performance analysis**

### 12 **Supercapacitor performance**

13 Electrochemical performance of the exfoliated TMD powders as supercapacitors is shown in Fig. 4(a) –  
14 (d).  
15



1  
2 **Figure 4. Electrochemical performance of exfoliated TMD electrodes in aqueous media as**  
3 **supercapacitor electrodes. (a)** CV of the exfoliated TMD electrodes in 1M aq. Na<sub>2</sub>SO<sub>4</sub> performed at a scan rate  
4 of 200 mV s<sup>-1</sup>, showing characteristic double layer capacitance behavior, **(b)** corresponding specific capacitances  
5 of the TMD electrodes at 5, 50, 100, 200 and 500 mV s<sup>-1</sup> with the MoS<sub>2</sub> electrode providing the best performance,  
6 **(c)** first cycle GCD curves of the exfoliated TMD electrodes obtained at a current density of 1 mA cm<sup>-2</sup>, **(d)**  
7 corresponding specific capacitances for the various TMD electrodes at current densities of 0.5, 1.0, 1.5 and  
8 2.0 mA cm<sup>-2</sup>, with MoS<sub>2</sub> demonstrating superior performance.

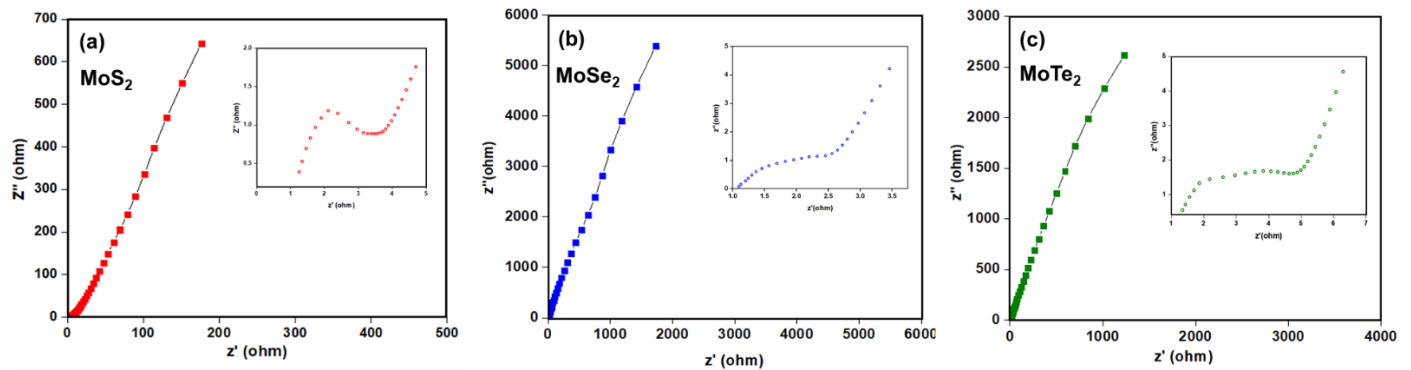
1  
2 Fig. 4(a) shows the CV results from exfoliated TMD electrodes collected at a  $200 \text{ mV s}^{-1}$  scan rate. All  
3 the samples exhibit a rectangular shaped CV curve indicating double layer capacitive behavior and  
4 suggesting that charge is stored along the electrode surface. It is observed that greater electrochemical  
5 surface areas obtained as a consequence of the layered, therefore, enhances the ability to store the  
6 charge at the interfaces. Increasing scan rates produced larger areas enclosed by the CV curve along  
7 with higher peak currents; however, no distinct redox peaks were observed. Fig. 4(b) shows the  
8 capacitances obtained for the same samples at CV scan rates from 5-500  $\text{mV s}^{-1}$ . Results demonstrate  
9 that  $\text{MoS}_2$  performs the best, providing a maximum areal capacitance of  $60.25 \text{ mF cm}^{-2}$ .

10 Figure 4(c) shows the first cycle GCD curves of the exfoliated TMD electrodes. The symmetric GCD  
11 curves correspond to a reversible electrochemical process with reduced hysteresis losses [34]. Here  
12 too, the  $\text{MoS}_2$  sample performs better than the others, with a maximum areal capacitance of  
13  $22.5 \text{ mF cm}^{-2}$  at a current density of  $0.5 \text{ mA cm}^{-2}$ . This can be attributed to the quality of exfoliation  
14 leading to better electrochemical properties of  $\text{MoS}_2$ , which fits well with the cross-sectional images  
15 seen in Fig. 3. Fig. 4(d) shows that the areal capacitances converge to similar values for all the samples  
16 at high current rates ( $\sim 2 \text{ mA cm}^{-2}$ ). This can be attributed to the significantly reduced ionic diffusion  
17 at such high current rates. These results corroborate ab-initio studies of  $\text{MoSe}_2$  electrodes as  
18 supercapacitors for Na-ion systems [35].

19 The capacitance values obtained in this manuscript represent the lower limit for the exfoliated TMD  
20 samples. This is because the samples were directly used after the exfoliation process without optimizing  
21 for the quality of output, i.e. quality and number of layers formed. Also, though characterization  
22 techniques demonstrate no impurity phases present, there may be electrochemically competing phases  
23 present which may not have been detected. A post-exfoliation "cleansing" of the TMD samples may  
24 also improve the capacitance.

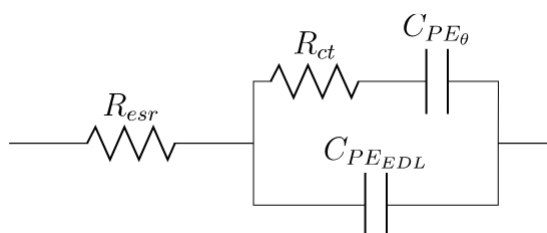
## 26 **Electrochemical impedance spectroscopy**

1 EIS was performed for further understanding the electrochemical behavior of the materials synthesized.  
 2 From figure 5 the Nyquist plot shows that for the three TMD/rGO materials studied, the semi-circle, at  
 3 the high-frequency region, is attributed to pseudocapacitive and double-layer (EDL) processes.  
 4 Importantly, one fact that may contribute towards the fast-charge faradaic processes for TMDs is the  
 5 fact that such species possesses different oxidation states [36]. Thus, the capacitance may be a  
 6 combination of EDL and faradaic charge storage processes [37].



7  
 8 **Figure 5. Electrochemical impedance spectra of the exfoliated TMD/rGO composite anodes. (a), (b) and**  
 9 **(c)** represent the EIS of the MoS<sub>2</sub>/rGO, MoSe<sub>2</sub>/rGO and MoTe<sub>2</sub>/rGO samples respectively, performed in aqueous  
 10 1M Na<sub>2</sub>SO<sub>4</sub> solution. All samples exhibit the characteristic inverted semicircle in the high frequency regime and a  
 11 linear trajectory in the low frequency regime.

12  
 13 The canonical circuit, proposed by Tilak *et al*, was employed to simulated the results [38]. This circuit,  
 14 as shown in schematic 1, is composed by the following elements: bulk equivalent series resistance of  
 15 the solution ( $R_{esr}$ ), charge transfer resistance ( $R_{ct}$ ), capacitance of the electric double layer ( $C_{PE\ EDL}$ ),  
 16 and the capacitance related to the pseudocapacitive reactions ( $C_{PE\theta}$ ) [39]. It is worth mentioning that  
 17 the capacitors in parallel ( $C_{PE\ EDL}$  and  $C_{PE\theta}$ ) are equivalent to  $Z_{CPE} = 1/Y_0(j\omega)^n$ , variable which accounts  
 18 for the dispersion phenomena inherent from electrodes surface, which are non-homogeneous; and for  
 19 the adsorption of ions from the electrolyte. Thus, these processes are simulated and quantified within  
 20 the range  $0 \leq n \leq 1$ .



**Schematic 1. Equivalent circuit corresponding to the EIS analysis, consisting of the individual resistive and capacitive components.**

From the circuit above, it is possible to obtain the contributions by each parameter i.e. bulk equivalent series resistance of the solution ( $R_{esr}$ ), charge transfer resistance ( $R_{ct}$ ), capacitance of the electric double layer ( $C_{PE\ EDL}$ ) and the capacitance related to the pseudocapacitive reactions ( $C_{PE\theta}$ ) and these values are provided in the table below.

Impedance element	MoS <sub>2</sub>	MoSe <sub>2</sub>	MoTe <sub>2</sub>
$R_{esr}$ ( $\Omega$ )	0.905	1.20	0.684
$R_{ct}$ ( $\Omega$ )	4.15	3.86	5.32
$C_{PE\ EDL} - Y_{EDL}$ ( $\mu\Omega^{-1}\cdot s^n$ )	32.9 (n = 0.702)	14.3 (n = 0.891)	31.1 (n = 0.67)
$C_{PE\theta} - Y_{\theta}$ ( $\mu\Omega^{-1}\cdot s^n$ )	387 (n = 0.763)	22.2 (n = 0.819)	61.5 (n = 0.80)

**Table 1. Listing of values of the individual resistive and capacitive components for each exfoliated TMD/rGO composite.**

### Battery performance

The performance of the TMD composite papers as anodes in Na/Na<sup>+</sup> half cells are provided in Fig. 6(a) - (g).

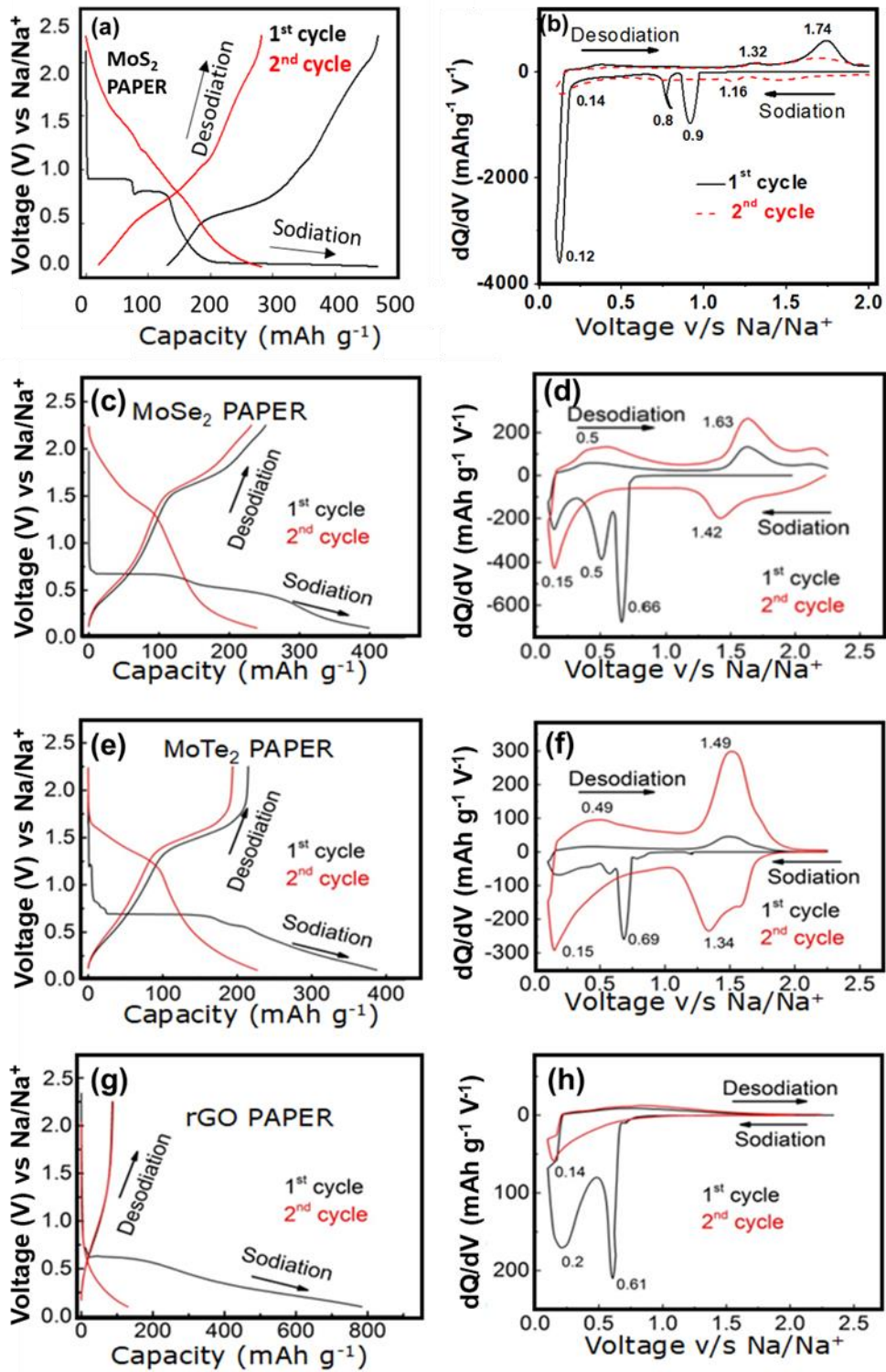


Figure 6. Electrochemical performance of TMD composite electrodes in Na/Na<sup>+</sup> half-cell. (a), (c), (e)

1 and **(g)** are the GCD curves of first and second cycles for the MoS<sub>2</sub>, MoSe<sub>2</sub>, MoTe<sub>2</sub> and rGO electrodes  
2 demonstrating their characteristic behavior towards Na<sup>+</sup> ion interaction, **(b)**, **(d)**, **(f)** and **(h)** are the  
3 corresponding dQ/dV plots of the composite TMD electrodes exhibiting the characteristic sodiation and desodiation  
4 peaks. (1 mAh g<sup>-1</sup> = 3.6 C g<sup>-1</sup>). Permission for reuse of data for figures (b), (g) and (h) obtained from ACS  
5 publications [23].

6  
7 Fig. 6(a), (c), and (e) and (g) are the first and second cycle GCD curves for the exfoliated TMD  
8 electrodes (MoS<sub>2</sub>, MoSe<sub>2</sub> and MoTe<sub>2</sub>) and the rGO electrodes respectively. The exfoliated MoS<sub>2</sub>, MoSe<sub>2</sub>  
9 and the MoTe<sub>2</sub> composite paper samples demonstrate first cycle sodiation (discharge) capacities of  
10 468.84 mAh g<sup>-1</sup> (1687.82 C g<sup>-1</sup>), 399.1 mAh g<sup>-1</sup> (1436.76 C g<sup>-1</sup>) and 387.36 mAh g<sup>-1</sup> (1394.49 C g<sup>-1</sup>)  
11 respectively, whereas their charge (desodiation) capacities are 512.25 mAh g<sup>-1</sup> (1844.1 C g<sup>-1</sup>),  
12 251.86 mAh g<sup>-1</sup> (906.73 C g<sup>-1</sup>) and 214.62 mAh g<sup>-1</sup> (772.66 C g<sup>-1</sup>) respectively. These charge capacities  
13 are approximately 2.5-3 times greater than that of the rGO electrode, which delivers a first cycle charge  
14 capacity of 81.5 mAh g<sup>-1</sup> (293.4 C g<sup>-1</sup>) as observed in Fig. 6(h). The authors would like to point out  
15 that these capacities are for free-standing TMD composite paper electrodes without any additive binder  
16 contributions. Also, the capacities obtained in the present manuscript are comparatively higher than  
17 some of the values that have been reported in the literature [40, 41].

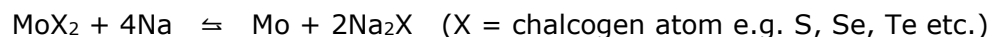
18 However, the rGO paper showed significantly higher charge capacity than commercial graphite (293.4  
19 C g<sup>-1</sup> versus ~126 C g<sup>-1</sup>) for the Na/Na<sup>+</sup> half-cell [42]. The voltage profile curves showed that the  
20 oxidation/reduction mechanism of TMD composite electrodes with respect to sodium exhibited two  
21 distinct plateaus and were very different when compared to the sloped rGO discharge curve. Differential  
22 capacity (dQ/dV) curves were plotted (Fig. 6 (b), (d), (f), (h)) to study the Na<sup>+</sup> ion interaction with the  
23 TMD and the rGO electrodes in greater detail. Since each peak corresponds to a specific reaction and  
24 certain peaks disappeared after the first cycle, those peaks (e.g. 0.5 V and 0.6 V for MoSe<sub>2</sub>, 0.69 V for  
25 MoTe<sub>2</sub>) can be ascribed to the formation of a solid electrolyte interface layer<sup>15</sup>. In the second cycle, all  
26 TMD electrodes showed two insertion peaks (~0.15 V and ~1.34 V to 1.46 V) and two extraction peaks  
27 (~0.5 and ~1.5 V to 1.7 V), which indicates distinct sodiation and desodiation in the TMD composite

1 electrodes.

2 From Fig. 6(a) MoS<sub>2</sub> demonstrates a two-step interaction with Na<sup>+</sup> ions, around ~0.9 V and ~0.75 V  
3 whereby intercalation of the cations take place into the ordered MoS<sub>2</sub> structure take place and a  
4 conversion reaction which causes MoS<sub>2</sub> to disintegrate into Mo and Na<sub>2</sub>S, and this has been reported  
5 in a previous report [23].

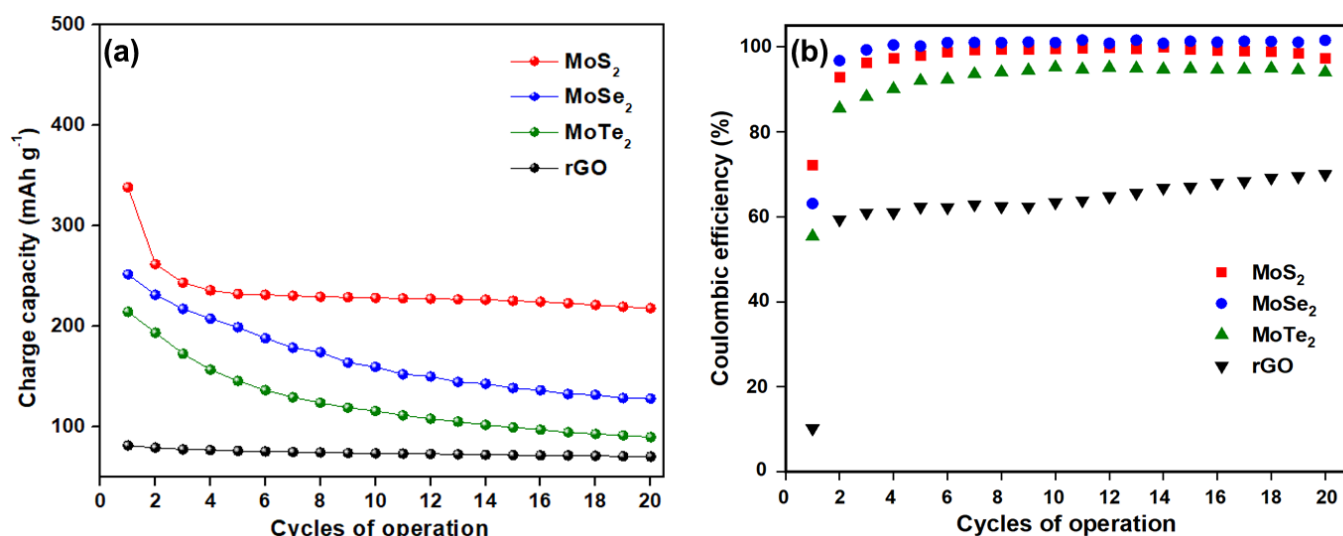
6 For MoSe<sub>2</sub>, ionic interaction with the structure results in its transformation from a semiconductor to a  
7 metal. Wang et al have demonstrated that when Na<sup>+</sup> ions intercalate into MoSe<sub>2</sub>, equal amounts of  
8 electrons also enter to maintain overall electrical neutrality and these electrons insert themselves into  
9 the t<sub>2g</sub> orbitals of Mo [25]. It is this that results in the transition to a metallic stage. Also, it has been  
10 shown that Na<sup>+</sup> ion intercalation can occur at two different sites in the MoSe<sub>2</sub> lattice: at a tetrahedral  
11 or an octahedral location. For MoSe<sub>2</sub>, the plateau at approximately 0.65 V corresponds to formation of  
12 Na<sub>x</sub>MoSe<sub>2</sub> whereas the other plateau at around 0.4 V corresponds to reduction of Mo<sup>4+</sup> to Mo and the  
13 formation of Na<sub>2</sub>Se [25].

14 The reaction mechanism is similar for MoTe<sub>2</sub>, also has a plateau corresponding to formation of metallic  
15 Mo and Na<sub>2</sub>Te [43]. The conversion reaction in this case is as follows:



17 It is noticed that all the TMD samples undergo a large first cycle capacity loss (especially MoS<sub>2</sub>), this is  
18 attributed to the SEI layer formation which impedes the charge transfer process initially. Also, structural  
19 changes occur during the initial processes as a result of the transformation process and side reactions  
20 with the electrolyte also contributes to first cycle loss. It is to be also noted that the difference in the  
21 cathodic and anodic peak locations for the TMDs with different chalcogen atoms are due to interfacial  
22 Na<sup>+</sup> ion storage, interaction/storage of Na<sup>+</sup> ions in different defective sites of each crystal and its  
23 constituent layers [44]. It is also understood that the presence of rGO enhances the performance of  
24 these exfoliated TMDs. rGO not only increases electronic conductivity, they also help prevent the  
25 restacking of the exfoliated TMD layers by acting as support and relieving the stress produced to the  
26 cell cycling [45, 46].

1 The rGO electrode only showed a broad plateau during the extraction half, indicating insufficient  
2 intercalation.



3  
4 **Figure 7. Capacity retention and coulombic efficiency curves. (a)** capacity retention trend and **(b)**  
5 coulombic efficiency trends showing the superior performance of TMD composite electrodes over standalone rGO  
6 electrode.

7  
8 Capacity retention data for various electrodes up to 20 cycles is presented in Fig. 7(a). After the  
9 completion of 20 cycles, MoS<sub>2</sub> demonstrated a capacity retention of ~83 % (leaving aside the first cycle  
10 loss) followed by MoSe<sub>2</sub> (63.44 %) and MoTe<sub>2</sub> (53.98 %). Furthermore, the TMD electrodes reached  
11 near 100 % cycling efficiency after the second discharge and remained constant up to the 20<sup>th</sup> cycle.  
12 Therefore, an analysis of the GCD and preliminary cell cycling results demonstrate the promise of our  
13 novel exfoliated free-standing TMD materials as negative electrodes for SIB applications. Additionally,  
14 as seen in figure 7(b), all TMD electrodes showed first cycle efficiency in excess of ~50 % compared  
15 to rGO, which demonstrated only 10.16 %.

## 17 Conclusion

18 A superacid-based technique was utilized to successfully exfoliate Mo-based layered TMDs. Detailed

1 structural and elemental characterization indicates the formation of phase pure few-layered TMD  
2 nanosheets, thereby demonstrating the efficacy of the process. The characterization process has also  
3 shown that sheets are usually homogenous and the acid-based process has not resulted in any  
4 dissolution of the material. The exfoliated sheets were then combined with rGO to form composite  
5 paper electrodes for electrochemical energy storage applications.

6 For both supercapacitor and battery configuration, all the TMD composite electrodes performs better  
7 than rGO providing an initial charge capacity of 468.84 mAh g<sup>-1</sup>, 399.10 mAh g<sup>-1</sup> and 387.36 mAh g<sup>-1</sup>  
8 for MoS<sub>2</sub>, MoSe<sub>2</sub> and MoTe<sub>2</sub> respectively. TMD electrodes also provide steady coulombic efficiencies  
9 (close to 100 % after a few cycles) and capacities values at least ~2.5 to 3 times than neat rGO  
10 electrode. The electrochemical analysis, especially the incremental capacity curves illustrate the Na<sup>+</sup>  
11 ion interaction mechanisms in the TMDs, with the transformation reaction regimes clearly distinguished  
12 for each electrode. The results offer promise for use of TMD-based electrodes in electrochemical energy  
13 storage systems.

## 14 **Data accessibility**

15 Data available from the Dryad Digital Repository at [47]: <https://doi:10.5061/dryad.tv2tk65>.

16 Reviewer URL: <https://datadryad.org/review?doi=doi:10.5061/dryad.tv2tk65>

## 17 **Competing Interest**

18 We have no competing interests.

## 19 **Acknowledgment**

20 This work is supported in part by National Science Foundation grant # 1454151.

## 21 **Author contribution**

22 J.T. and S.M. performed supercapacitor testing. L.D. prepared composite paper electrodes and battery  
23 tests. G.S. assisted L.D. with cell assembly. E.M and J.H. performed electron microscopy and elemental  
24 analysis/mapping. G.S. conceived the idea, designed the experiments, and co-wrote the manuscript  
25 with S.M., D.S. performed the impedance spectra experiments. All authors discussed the results and  
26 commented or revised the manuscript.  
27

## 1 Ethics requirement

2 No ethical assessments were required to be completed prior to this research. No animal ethical  
3 assessments were required to be performed for this research. No fieldwork was required to be  
4 performed for this research.

## 6 References

- 8 1 Gogotsi, Y. 2014 What Nano Can Do for Energy Storage. *ACS Nano*. **8**, 5369-5371.  
9 2 Casas, C. d. l., Li, W. 2012 A review of application of carbon nanotubes for lithium ion battery anode material.  
10 *Journal of Power Sources*. **208**, 74-85.  
11 3 Etacheri, V., Marom, R., Elazari, R., Salitra, G., Aurbach, D. 2011 Challenges in the development of advanced Li-  
12 ion batteries: a review. *Energy and Environmental Science*. **4**, 3243-3262.  
13 4 Goodenough, J. B., Park, K.-S. 2013 The Li-Ion Rechargeable Battery: A Perspective. *Journal of the American*  
14 *Chemical Society*. **135**, 1167-1176.  
15 5 Wu, Z.-S., Ren, W., Xu, L., Li, F., Cheng, H.-M. 2011 Doped Graphene Sheets As Anode Materials with Superhigh  
16 Rate and Large Capacity for Lithium Ion Batteries. *ACS Nano*. **5**, 5463-5471.  
17 6 Armand, M., Tarascon, J. M. 2008 Building better batteries. *Nature*. **451**, 652-657.  
18 7 Nishi, Y. Lithium ion secondary batteries; past 10 years and the future. *Journal of Power Sources*. **100**, 101-106.  
19 8 Slater, M. D., Kim, D., Lee, E., Johnson, C. S. 2013 Sodium-Ion Batteries. *Advanced Functional Materials*. **23**,  
20 947-958.  
21 9 Wu, N., Lyu, Y.-C., Xiao, R.-J., Yu, X., Yin, Y.-X., Yang, X.-Q., Li, H., Gu, L., Guo, Y.-G. 2014 A highly  
22 reversible, low-strain Mg-ion insertion anode material for rechargeable Mg-ion batteries. *Asia Materials*. **6**, 1-7.  
23 10 Jayaprakash, N., Das, S. K., Archer, L. A. 2011 The rechargeable aluminum-ion battery. *Chemical*  
24 *Communications*. **47**, 12610-12612.  
25 11 Liu, Y., Fan, F., Wang, J., Liu, Y., Chen, H., Jungjohann, K. L., Xu, Y., Zhu, Y., Bigio, D., Zhu, T., *et al.* 2014 In  
26 Situ Transmission Electron Microscopy Study of Electrochemical Sodiation and Potassiation of Carbon Nanofibers.  
27 *Nano letters*. **14**, 3445-3452.  
28 12 Palomares, V., Serras, P., Villaluenga, I., Hueso, K. B., Carretero-González, J., Rojo, T. 2012 Na-ion batteries,  
29 recent advances and present challenges to become low cost energy storage systems. *Energy and Environmental*  
30 *Science*. **5**, 5884-5901.  
31 13 Palacin, M. R. 2009 Recent advances in rechargeable battery materials: a chemist's perspective. *Chemical Society*  
32 *Reviews*. **38**, 2565-2575.  
33 14 Mukherjee, S., Ren, Z., Singh, G. 2018 Beyond Graphene Anode Materials for Emerging Metal Ion Batteries and  
34 Supercapacitors. *Nano-Micro Letters*. **10**,  
35 15 Kim, S.-W., Seo, D.-H., Ma, X., Ceder, G., Kang, K. 2012 Electrode Materials for Rechargeable Sodium-Ion  
36 Batteries: Potential Alternatives to Current Lithium-Ion Batteries. *Advanced Energy Materials*. **2**, 710-721.  
37 16 Yabuuchi, N., Kubota, K., Dahbi, M., Komaba, S. 2014 Research Development on Sodium-Ion Batteries.  
38 *Chemical Reviews*. **114**, 11636-11682.  
39 17 Aricò, A. S., Bruce, P., Scrosati, B., Tarascon, J. M., Schalkwijk, W. v. 2005 Nanostructured materials for  
40 advanced energy conversion and storage devices. *Nature Materials*. **4**, 366-377.  
41 18 Ellis, B. L., Nazar, L. F. 2012 Sodium and sodium-ion energy storage batteries. *Current Opinion in Solid State*  
42 *and Materials Science*. **16**, 168-177.

- 19 Chhowalla, M., Shin, H. S., Eda, G., Li, L. J., Loh, K. P., Zhang, H. 2013 The chemistry of two-dimensional layered transition metal dichalcogenide nanosheets. *Nature Chemistry*. **5**, 263-275.
- 20 Choi, W., Choudhary, N., Han, G. H., Park, J., Akinwande, D., Lee, Y. H. 2017 Recent development of two-dimensional transition metal dichalcogenides and their applications. *Materials Today*. **20**, 116-130.
- 21 Mukherjee, S., Singh, G. 2019 Two-Dimensional Anode Materials for Non-lithium Metal-Ion Batteries. *ACS Applied Energy Materials*. **2**, 932-955. (10.1021/acsaem.8b00843)
- 22 Khalil, A., Liu, Q., He, Q., Xiang, T., Liu, D., Wang, C., Fang, Q., Song, L. 2016 Metallic 1T-WS<sub>2</sub> nanoribbons as highly conductive electrodes for supercapacitors. *RSC Advances*. **6**, 48788-48791.
- 23 David, L., Bhandavat, R., Singh, G. 2014 MoS<sub>2</sub>/Graphene Composite Paper for Sodium-Ion Battery Electrodes. *ACS Nano*. **8**, 1759-1770.
- 24 Ge, P., Fouletier, M. 1988 Electrochemical Intercalation of Sodium in Graphite. *Solid State Ionics*. **28-30**, 1172-1175.
- 25 Wang, H., Lan, X., Jiang, D., Zhang, Y., Zhong, H., Zhanga, Z., Jiang, Y. 2015 Sodium storage and transport properties in pyrolysis synthesized MoSe<sub>2</sub> nanoplates for high performance sodium-ion batteries. *Journal of Power Sources*. **283**, 187-194.
- 26 Jr, W. S. H., Offeman, R. E. 1958 Preparation of Graphitic Oxide. *Journal of the American Chemical Society*. **80**, 1339-1339.
- 27 Cunningham, G., Lotya, M., Cucinotta, C. S., Sanvito, S., Bergin, S. D., Menzel, R., Shaffer, M. S. P., Coleman, J. N. 2012 Solvent Exfoliation of Transition Metal Dichalcogenides: Dispersibility of Exfoliated Nanosheets Varies Only Weakly between Compounds. *ACS Nano*. **6**, 3468-3480.
- 28 Nicolosi, V., Chhowalla, M., Kanatzidis, M. G., Strano, M. S., Coleman, J. N. 2013 Liquid Exfoliation of Layered Materials. *Science*. **340**,
- 29 Crane, M. J., Lim, M. B., Zhou, X., Pauzauskie, P. J. 2017 Rapid synthesis of transition metal dichalcogenide-carbon aerogel composites for supercapacitor electrodes. *Microsystems and Nanoengineering*. **3**,
- 30 Karade, S. S., Sankapal, B. R. 2017 Two dimensional cryptomelane like growth of MoSe<sub>2</sub> over MWCNTs: Symmetric all-solid-state supercapacitor. *Journal of Electroanalytical Chemistry*. **802**, 131-138.
- 31 Chen, J. M., Wang, C. S. 1974 Second Order Raman Spectrum of MoS<sub>2</sub>. *Solid State Communications*. **14**, 857-860.
- 32 Windom, B., Sawyer, W. G., Hahn, D. A. 2011 Raman Spectroscopic Study of MoS<sub>2</sub> and MoO<sub>3</sub>. *Tribological Letters*. **42**, 301-310.
- 33 Tonndorf, P., Schmidt, R., Böttger, P., Zhang, X., Börner, J., Liebig, A., Albrecht, M., Kloc, C., Gordan, O., Zahn, D. R. T., *et al.* 2013 Photoluminescence emission and Raman response of monolayer MoS<sub>2</sub>, MoSe<sub>2</sub>, and WSe<sub>2</sub>. *Optics Express*. **21**, 4908-4916.
- 34 Ratha, S., Rout, C. S. 2013 Supercapacitor Electrodes Based on Layered Tungsten Disulfide-Reduced Graphene Oxide Hybrids Synthesized by a Facile Hydrothermal Method. *Applied Materials and Interfaces*. **5**, 11427-11433.
- 35 Zhao, X., Cai, W., Yang, Y., Song, X., Neale, Z., Wang, H.-E., Sui, J., Cao, G. 2018 MoSe<sub>2</sub> nanosheets perpendicularly grown on graphene with Mo-C bonding for sodium-ion capacitors. *Nano Energy*. **47**, 224-234.
- 36 Soon, J. M., Loh, K. P. 2007 Electrochemical Double-Layer Capacitance of MoS<sub>2</sub> Nanowall Films. *Electrochemical and Solid State Letters*. **10**,
- 37 Nunes, W. G., Vicentini, R., Silva, L. M. D., Costa, L. H., Tadeu, T., Zanin, H. 2018 Surface and Electrochemical Properties of Radially Oriented Multiwalled Carbon Nanotubes Grown on Stainless Steel Mesh. *Journal of the Electrochemical Society*. **165**, A3684-A3696.
- 38 Tilak, B. V., Chen, C. P., Rangarajan, S. K. 1992 A model to characterize the impedance of electrochemical capacitors arising from reactions of the type. *Journal of Electroanalytical Chemistry*. **324**, 405-414.

- 1 39 Hsieh, C. T., Chen, W. Y., Cheng, Y. S. 2010 Influence of oxidation level on capacitance of electrochemical  
2 capacitors fabricated with carbon nanotube/carbon paper composites. *Electrochimica Acta*. **55**, 5294-5300.
- 3 40 Panda, M. R., K., A. R., Bao, Q., Mitra, S. Year MoTe<sub>2</sub>, A novel anode material for sodium ion battery. American  
4 Institute of Physics; 2018; 2018.
- 5 41 Shi, Z. T., Kang, W., Xu, J., Sun, L. L., Wu, C., Wang, L., Yu, Y. Q., Yu, D. Y. W., Zhang, W., Lee, C. S. 2015  
6 In Situ Carbon - Doped Mo(Se<sub>0.85</sub>S<sub>0.15</sub>)<sub>2</sub> Hierarchical Nanotubes as Stable Anodes for High - Performance  
7 Sodium - Ion Batteries. *Small*. **11**, 5667-5674.
- 8 42 Moriwake, H., Kuwabara, A., Fisher, C. A. J., Ikuhara, Y. 2017 Why is sodium-intercalated graphite unstable?  
9 *RSC Advances*. **7**, 36550-36554.
- 10 43 Cho, J. S., Ju, H. S., Lee, J.-K., Kang, Y. C. 2017 Carbon/two-dimensional MoTe<sub>2</sub> core/shellstructured  
11 microspheres as an anode material for Na-ion batteries. *Nanoscale*. **9**, 1942-1950.
- 12 44 Kong, D., He, H., Song, Q., Wang, B., Lv, W., Yang, Q.-H., Zhi, L. 2014 Rational design of MoS<sub>2</sub>@graphene  
13 nanocables: towards high performance electrode materials for lithium ion batteries. *Energy and Environmental  
14 Science*. **7**, 3320-3335.
- 15 45 Romil Bhandavat, L. D., Gurpreet Singh. 2012 Synthesis of Surface-Functionalized WS<sub>2</sub> Nanosheets and  
16 Performance as Li-Ion Battery Anodes. *The Journal of Physical Chemistry Letters*. 1523-1530.
- 17 46 Lamuel David, R. B., and Gurpreet Singh. 2014 MoS<sub>2</sub>/Graphene Composite Paper for Sodium-Ion Battery  
18 Electrodes. *ACS Nano*. 1759-1770.
- 19 47 Mukherjee, S., Turnley, J., Mansfield, E., Holm, J., David, L., Singh, G. 2019 Data from: Exfoliated transition  
20 metal dichalcogenide (TMD) nanosheets for supercapacitor and sodium ion battery applications *Dryad Digital  
21 Repository*. (10.5061/dryad.tv2tk65)  
22